Energy Engineering

Tech Science Press

https://doi.org/10.32604/ee.2026.081082

ARTICLE

A Novel Control-Protection Coordination Strategy of Power Lines Connected with Inverter-Based Resources

Sumei Liu[1,*], Jizeng Wu[1], Yinghong Zhang[2] and Ran Zheng[3]

[1]College of Engineering, Beijing Forestry University, Beijing, China
[2]Tianshui Power Supply Company, State Grid Gansu Electric Power Company, Tianshui, China
[3]Jinhua Power Supply Company, State Grid Zhejiang Electric Power Company, Jinhua, China

*Corresponding Author: Sumei Liu. Email: smliu@bjfu.edu.cn

Received: 23 February 2026; Accepted: 02 April 2026; Published: 27 May 2026

ABSTRACT: The unique fault current characteristics of inverter-based resources (IBRs) result in a variable angle of the additional impedance for conventional distance protection, causing failure to operate for internal faults and maloperation for external faults. To address this issue, a novel control-protection coordinated strategy is proposed. The positive-sequence current references of IBRs' inverter control strategy are reset, based on the relationship between the current on the high-voltage side of the transformer and that of the fault-point current. Under such control, the additional impedance angle can be effectively maintained at a constant value. On this basis, a single-ended protection principle immune to the additional impedance is developed. The proposed control-protection coordinated strategy can effectively identify internal and external faults under high-penetration IBRs integration, without substantially modifying the existing inverter control and protection framework. Compared with existing control-protection coordinated strategies, the proposed improved control strategy will not affect the stability of inverter control, nor will it generate additional harmonics. The proposed protection strategy still adopts conventional power-frequency voltage and current quantities for fault identification, facilitating its implementation.

KEYWORDS: Distance protection; control-protection coordination; additional impedance

1 Introduction

With the growing penetration of inverter-based resources (IBRs, e.g., photovoltaics (PV) plants, energy storage (ES), and permanent magnet direct-driven (PMDD) wind farm), the fault current characteristics of the connected grids are fundamentally altered [1–3]. As a result, significant challenges are presented to existing protection strategies, particularly for distance protection. Some typical cases are: (1) The distance protection for a 110 kV line connected with a wind farm in North China maloperated during a reverse external fault [4]; (2) A 110 kV feeder of 220 kV substation in Central China incorrectly operated during external faults due to impedance measurement distortion caused by wind farm integration [5]. Thus, widespread attention is paid to the mis-operation issues in distance protection caused by IBR integration [6–8].

To tackle the aforementioned issues, most studies develop either enhanced protection criteria or novel criteria based on the unique fault features of IBRs. Based on the assumption that the angle of the IBRs' short-circuit current is consistent with that of the fault-point current, in [9] the measured impedance is recalculated for the adaptive Zone II distance protection principle. Although the protection can eliminate the influence of fault resistance on the measured impedance, its performance is significantly affected by the angle characteristics of fault current from IBRs. In fact, the mentioned angle characteristics are governed by the IBRs' control strategy. Ref. [10] also develops an adaptive mho characteristic-based distance protection to mitigate the adverse effect of fault resistance caused by the IBRs' integration. The protection operation zone varies with the additional impedance angle. However, the additional impedance angle is obtained based on the assumption that IBRs do not provide negative-sequence current. Ref. [11] proposes an adaptive distance relay setting based on specific positive and negative sequence impedances of the IBRs. The impedance characteristic depends on the IBRs' specific control strategy, which adopts a dual-sequence reference frame to mitigate the dc-link oscillation and reduce the negative-sequence voltage. To sum up, the effectiveness of the aforementioned protection strategies is influenced by the IBRs' fault characteristics. The IBRs' fault characteristics are various with their control strategies [12].

Different from the previous studies, some control-protection coordination strategies are also adopted. These strategies mainly modify the control strategies to restore fault identification of distance protection, or improve both the control strategies and the distance protection criteria simultaneously. In terms of modifying the control strategies of IBRs, in [13] the positive reference values of current control loops for IBRs are reset to emulate the phase relationship between the positive- and negative-sequence currents supplied by synchronous generators (SGs). This approach can prevent incorrect operation of distance relays for IBR-connected lines, but it is only applicable to asymmetrical faults. In [14], the current references of IBRs are also adjusted so that the measured reactance of the distance relay is mostly equal to the actual line reactance under various fault types. However, the limited amplitude of fault currents from IBRs easily leads to an excessively large resistive component in the measured impedance [15,16], resulting in incorrect operation of the protection during high-resistance faults. In fact, the performance of distance protection is affected by the amplitude relationship between short-circuit currents at both ends of IBR-connected lines [17]. The larger the amplitude difference is, the greater the error between the measured impedance and the actual line impedance becomes. Whereas, the short-circuit current amplitude supplied by IBRs is inherently small (only 1.2–1.5 times the rated current) [18], which results in a high risk of incorrect operation for conventional distance protection.

In terms of developing the protection principles on the basis of improving the IBRs' control strategies, most studies focus on two-terminal differential protection [19–21]. Nevertheless, the two-terminal protection relies on communication, and it is difficult to implement. Therefore, some single-terminal protection strategies are also studied for IBR-connected lines by modifying inverters' control strategies. Ref. [22] proposes an improved time-domain distance protection based on adaptive high-frequency voltage control. In order to accurately calculate the fault distance, a 400 Hz negative-sequence voltage signal is modulated via the inverter's negative-sequence control. However, this study is aimed at an MMC-based offshore AC network. Ref. [23] also proposes an improved time-domain distance protection strategy by injecting a 20 Hz modulated voltage signal into IBRs' inverter control. However, the continuous injection may cause grid harmonic distortion. And the signals' characteristics may also be influenced by the power grid topologies, their corresponding parameters, and so on [24]. As a result, it impairs the performance of protection strategies based on these signals.

Different from the mentioned protection strategies based on the characteristic signals, the negative sequence fault current of IBRs is altered by optimizing the inverters' control strategy in [25] in order to accurately identify the faulty distance. Such approach does not affect the power quality of the grid, but the presence of negative-sequence current can cause inverter control instability due to dc-link voltage fluctuations [26].

As analyzed above, the key issues to be addressed in designing a control-protection coordinated strategy include: (1) The improved control strategy can generate unique electrical quantities suitable for fault identification without compromising the control stability of the inverter; (2) The developed protection principle only requires local electrical quantities, independent of the fault conditions, IBRs' capacity, and so on. Aimed at these problems, in this manuscript a novel control–protection coordination strategy for transmission lines connected with IBRs is proposed. And its main contributions are summarized as follows:

(1) An enhanced control strategy for the IBRs' inverters is proposed through resetting positive-sequence current references to ensure that the additional impedance angle is reduced to zero. The adjusted current references do not compromise the inverter control stability.

(2) The proposed protection criterion belongs to single-ended quantity protection, which employs the reactance component of the measured impedance for estimating fault distance. Even under high-penetration IBRs integration scenarios, it can effectively mitigate the impact of fault resistance.

The rest of this paper is organized as follows. Section 2 qualitatively analyzes and reveals the relationship between IBRs' control strategies and the impedance measurement of distance protection. Section 3 proposes an enhanced control strategy for the IBRs' inverters and derives analytical expressions of fault-point current angles under different fault types by using only electrical quantity from the IBRs' side. Section 4 develops a novel single-ended protection criterion. Section 5 verifies the effectiveness of the proposed control strategy and protection criterion using PSCAD/EMTDC simulations.

2 The Challenges of Traditional Distance Protection Applied for the IBRs-Connected Lines

Here the conventional distance protection of the line connected with a photovoltaic (PV) power station is taken as an example to analyze its applicability. The grid-connected system topology of the PV power station is shown in Fig. 1. In Fig. 1, B_1 and B_2 represent the distance relay at both ends of the 110 kV line MN. And Z_s is the equivalent impedance of the grid.

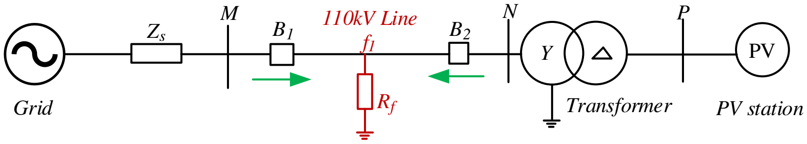

Figure 1: Grid-connected topology diagram of PV power station.

When the fault f_1 with fault resistance R_f occurs in Fig. 1, the measured impedance of distance relay B_2 on the PV station side can be expressed as

$$Z_{mN} = \frac{\dot{U}_{mN}}{\dot{I}_{mN}} = Z_{Nk} + \frac{\dot{I}_{mN} + \dot{I}_{mM}}{\dot{I}_{mN}} R_f = Z_{Nk} + \left| \frac{\dot{I}_f}{\dot{I}_{mN}} \right| \mathrm{e}^{j\alpha_{ad}} R_f = Z_{Nk} + Z_{\mathrm{ad}} \tag{1}$$

where Z_{Nk} denotes the actual impedance of the fault line. $\dot{U}_{mN}$ and $\dot{I}_{mN}$ represent the measured IBRs-side voltage and current, respectively. $\dot{I}_{mM}$ refers to grid-side current, while $\dot{I}_f = \dot{I}_{mN} + \dot{I}_{mM}$ is the fault-point current. Z_{ad} is the additional impedance of the distance delay B_2.

As shown in (1), the difference between measured impedance Z_{mN} and actual impedance Z_{Nk} is determined by the additional impedance Z_{ad}. The changing characteristics of Z_{ad} are influenced by the fault current $\dot{I}_{mN}$ provided by PV stations. Different from the SGs, the fault current amplitude provided by PV stations is limited and the corresponding current angle is governed by the inventor control strategy. Considering the impact of current amplitude, the ratio $|\dot{I}_f/\dot{I}_{mN}|$ is always greater than 1. Consequently, the additional impedance is consistently large even though R_f is small. Taking into account the effect of the short-circuit current angle, the additional impedance angle is various. The additional impedance angle, defined as the angle difference between the fault-point current and the IBR-side current ($\alpha_{ad} = \arg\left(\dot{I}_f\right) - \arg\left(\dot{I}_{mN}\right)$), varies with the short-circuit current angle. As a result, the reactance component of the measured impedance is identical to that of the actual impedance even if the fault resistance is constant. Owing to the constraint of the inverter's overcurrent capability, the maximum amplitude of the fault current provided by IBRs remains unchanged. Therefore, in order to improve the performance of distance delay, only the angle of the fault current can be adjusted. Next, the influence of the mentioned angle on the performance of traditional distance delay is analyzed in detail.

The sign of the additional impedance angle α_{ad} is governed by the angle relationship between the PV-side fault current and the fault-point current. Fig. 2 illustrates the variation range of α_{ad} with the change of the IBRs-side fault current. As shown in Fig. 2a, when the PV-side current leads the fault-point current, α_{ad} is a negative value. With the increase in the leading angle, α_{ad} decreases and gradually approaches −180°. This causes the measured impedance to be moved from the non-operating zone into the operating zone, leading to maloperation of the distance relay B_2 under the external faults.

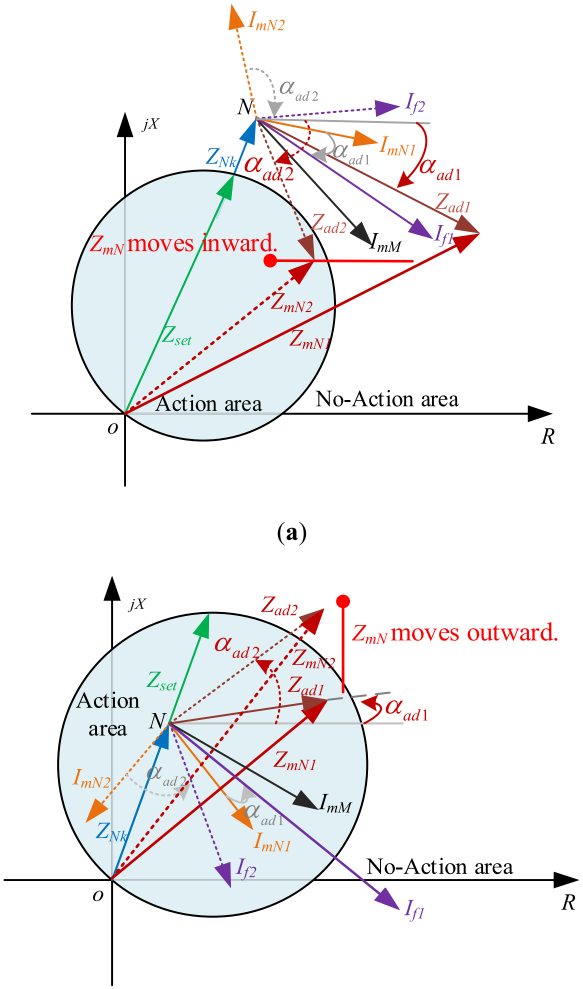

Figure 2: The variation range of the additional impedance angle with the change of the IBRs-side fault current. (**a**) the PV-side current leading the fault-point current; (**b**) the PV-side current lagging the fault-point current.

By contrast, as shown in Fig. 2b, when the PV-side fault current lags the fault-point current, α_{ad} is a positive value. With the increase in the lagging angle, α_{ad} increases and gradually approaches 180°. This causes the measured impedance to be moved from the operating zone into the non-operating zone, resulting in the distance relay B_2 failing to operate under the internal faults.

In summary, α_{ad} fluctuates within the range of $-180°$ to $180°$ due to variation in the angle of the PV-side fault current. In fact, according to the reactive power support requirements specified in the fault ride-through (FRT) code, the angle of the short-circuit current supplied by the IBRs is related to the voltage sag at the point of common coupling (PCC). The angle varies with the depth of voltage sag under different fault scenarios. As a result, the PV-side fault current may lead or lag the fault-point current.

3 An Enhanced Control Strategy for the IBRs' Inverters

From the above analysis, the variation of α_{ad} may result in maloperation or failure to operate of the traditional distance protection. To address the problem, in this section the control strategy of the IBRs' inverters is improved to align the angle of $\dot{I}_{mN}$ with that of $\dot{I}_f$. Consequently, α_{ad} becomes a constant and is no longer affected by the angle variation of $\dot{I}_{mN}$. Whereas, the angle of $\dot{I}_{mN}$ is determined by the current reference values of inverter's control-loop. Here, the relationship between current reference and fault-point current angle is firstly analyzed, then the reference values are deduced under fault types.

3.1 The Relationship between Positive-Sequence Current Reference and Fault-Point Current Angle

The control block diagram of the grid-connected IBRs is shown in Fig. 3. Considering that most inverters adopt a negative-sequence current suppression strategy during faults, in this paper the positive-sequence current references are reset to align the angle of the current $\dot{I}_{mN}$ with that of the fault-point current $\dot{I}_f$. As shown in Fig. 3, the positive-sequence current references for the improved inverter control strategy are mainly calculated by monitoring the voltage at bus N and the current $\dot{I}'_{mN}$ on the high-voltage side of the transformer.

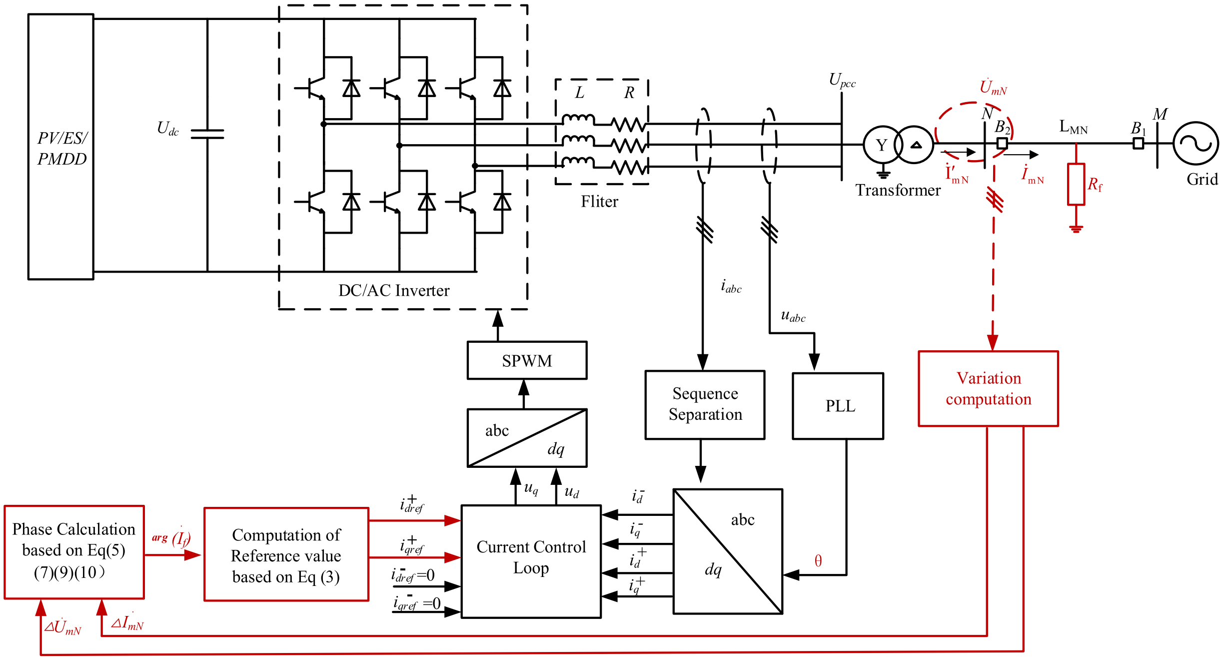

Figure 3: The control block diagram of the grid-connected IBRs.

As the line studied in this paper is the distance protection on the IBRs side of a dedicated IBRs-connected outgoing line, no intermediate taps, load branches or other power sources are connected between the high-voltage side of the grid-connected inverter transformer and bus N. Also, for the 110 kV medium and short-distance line, the distributed capacitive current is extremely small at power frequency, and its influence on the currents at both sides is negligible. Therefore, current continuity is maintained in the line section, and the current amplitude and phase remain consistent. Thus, it is considered that $\dot{I}'_{mN}$ is approximately equal to $\dot{I}_{mN}$. However, the aforementioned assumption may deviate if loads or distributed power sources are connected in the line, or if the line is of extra-high voltage and extra-long distance. Such deviations will be verified by subsequent simulations. The phase angle of the inverter output current is directly determined by the positive-sequence current references, i.e., $\arg\left(\dot{I}_{mN}\right) = \theta_v^+ - \arctan\left(\frac{i_{qref}^+}{i_{dref}^+}\right)$, where θ_v^+ is the angle of the positive-sequence voltage at the grid-connected bus. To ensure that the angle of $\dot{I}_{mN}$ is aligned with that of $\dot{I}_f$, the relationship between the fault-point current angle and the positive-sequence current reference is further obtained as follows.

$$\arg\left(\dot{I}_f\right) = \theta_v^+ + \arctan\left(\frac{i_{qref}^+}{i_{dref}^+}\right) \tag{2}$$

Further considering the overcurrent capacity limits of IBR inverters $\sqrt{\left(i_{dref}^+\right)^2 + \left(i_{qref}^+\right)^2} \le \mathrm{I}_{\mathrm{m}ax}$, the expression for the positive-sequence current reference is derived as follows.

$$\begin{cases} i_{dref}^+ = \mathrm{I}_{\mathrm{m}ax} \left| \cos\left(\arg\left(\dot{I}_f\right) - \theta_v^+\right) \right| \\ i_{qref}^+ = i_{dref}^+ \times \tan\left(\arg\left(\dot{I}_f\right) - \theta_v^+\right) \end{cases} \tag{3}$$

where $\mathrm{I}_{\mathrm{m}ax}$ is the maximum allowable current of the inverter. From (3), the accurate calculation of the reference value requires the fault current. However, the current angle at the fault point is difficult to obtain from the viewpoint of inverter control. Whereas the bus voltage and the transformer high-voltage-side current can be obtained through monitoring. To accurately calculate the current reference, it is necessary to analyze the relationship between the fault-point current, the bus voltage, and the transformer high-voltage-side current. However, the relationship varies under different fault types. The following mainly discusses the calculation method of the current reference under different fault types.

3.2 Calculation of the Positive-Sequence Current Reference under Different Fault Types

Considering that the fault-point current $\dot{I}_f$ exists only under fault conditions, the relationship between the fault-point current, the bus voltage, and the transformer high-voltage-side current is derived by establishing the fault-component equivalent network. The derivation of the fault-point current angle relies on the assumption that the grid-side positive-sequence equivalent impedance is much smaller than the IBR-side impedance (including the transformer and the line), i.e., $|Z_{s1}| << |Z_{IBR1} + Z_{MN1}|$. This assumption is justified by the inherent characteristics of the two sources. On the IBR side, the fault current is strictly limited by the inverter's overcurrent capability (typically 1.2–1.5 p.u.), which, from an equivalent circuit perspective, manifests as a large internal impedance. Additionally, the step-up transformer contributes a significant short-circuit impedance, with a typical short-circuit voltage of 10%–15%, further increasing Z_{IBR1}. On the grid side, transmission-level IBRs are commonly connected to strong grids, where the short-circuit ratio (SCR) exceeds 3, implying a relatively small Z_{s1}. Consequently, the assumption holds for the typical scenarios considered in this study.

(1) Three-Phase Fault

A three-phase fault is a symmetrical fault, and thus only positive-sequence components are considered. Fig. 4 shows the fault-component equivalent network under a three-phase fault.

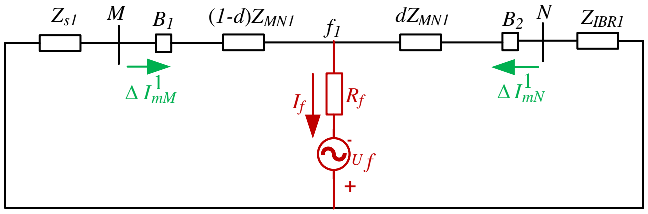

Figure 4: The fault component equivalent network under a three-phase fault.

According to Fig. 4, the fault-point current $\dot{I}_f$ is the sum of the grid-side and IBR-side fault current components, i.e., $\dot{I}_f = \Delta\dot{I}^1_{mM} + \Delta\dot{I}^1_{mN}$. Considering the limited fault current injection capability of IBRs, the fault current provided by the strong grid is considerably larger than that from the IBR side. Consequently, the impedance relationship $|Z_{s1}| << |Z_{IBR1} + Z_{MN1}|$ introduced at the beginning of this section is applicable. proposed earlier in this section is reasonably adopted. On the basis of the current division principle, the ratio between $\Delta\dot{I}^1_{mN}$ and $\dot{I}_f$ in Fig. 4 is derived as

$$\frac{\Delta \mathrm{I}^1_{mN}}{\dot{I}_f} = \frac{Z_{s1} + (1-d)\,Z_{MN1}}{Z_{s1} + Z_{MN1} + Z_{IBR1}} = \frac{Z_{s1} + (1-d)\,Z_{MN1}}{Z_{MN1} + Z_{IBR1}} \tag{4}$$

where Z_{s1} is the positive-sequence equivalent impedance of the grid; Z_{IBR1} is the positive-sequence equivalent impedance of the IBRs-side (including the transformer); d is the ratio of the actual faulted impedance to the total impedance of the line MN.

It is assumed that both the grid-side positive-sequence equivalent impedance and the line impedance satisfy $Z_{s1} = k_s Z_{MN1}$ (k_s is constant), The fault-point current angle can be derived from (4) as

$$\arg\left(\dot{I}_f\right) = \arg\left(\Delta\dot{I}^1_{mN} \times \frac{Z_{MN1} + Z_{IBR1}}{(1 + k_s - d)\,Z_{MN1}}\right) = \arg\left(\Delta\dot{I}^1_{mN} \times Z_{MN1} - \Delta\dot{U}^1_{mN}\right) - \varphi_{\text{set}} \tag{5}$$

where $\Delta\dot{U}^1_{mN} = -\Delta\dot{I}^1_{mN} \cdot Z_{IBR1}$ is the fault component of the voltage at the IBRs-side relay B_2. φ_{set} is the impedance angle of the protected line. According to (5), the fault-point current angle can be calculated from $\Delta\dot{I}^1_{mN}$ and $\Delta\dot{U}^1_{mN}$. Meanwhile, both $\Delta\dot{I}^1_{mN}$ and $\Delta\dot{U}^1_{mN}$ are electrical quantities on the IBRs-side, which makes it possible to improve inverter control.

(2) Phase to Phase Fault

A phase-to-phase fault is an unsymmetrical fault, and thus the positive-sequence and negative-sequence components should be considered. Fig. 5 shows the fault-component equivalent network under the phase-B-to-phase-C fault.

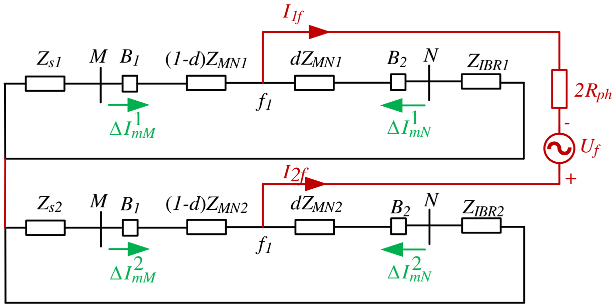

Figure 5: The fault component equivalent network under a phase-to-phase fault.

According to Fig. 5, the fault-point current under the phase-B-to-phase-C fault can be expressed as

$$\dot{I}_f = \dot{I}_B^{1f} + \dot{I}_B^{2f} = \dot{I}_A^{1f} e^{-j120^\circ} + \dot{I}_A^{2f} e^{j120^\circ} = \dot{I}_A^{1f}\left(e^{-j120^\circ} - e^{j120^\circ}\right) = \dot{I}_A^{1f}\left(-j\sqrt{3}\right) \tag{6}$$

where $\dot{I}_B^{1f}$ and $\dot{I}_B^{2f}$ are the phase-B currents at the fault point provided by the positive-sequence and negative-sequence networks. $\dot{I}_A^{1f}$ and $\dot{I}_A^{2f}$ are the healthy phase-A currents at the fault point provided by the positive-sequence and negative-sequence networks. As shown in (6), $\dot{I}_f$ is related to the phase-A current $\dot{I}_A^{1f}$ of the fault point provided by the positive-sequence network. In fact, the variation characteristics of $\dot{I}_A^{1f}$ under a phase-to-phase fault is consistent with those of the fault-point current under symmetrical faults. Therefore, combining with (5), the expression for the angle of the fault-point current can be obtained as follows.

$$\arg\left(\dot{I}_f\right) = \arg\left(\Delta\dot{I}_{mN}^1 \times Z_{MN1} - \Delta\dot{U}_{mN}^1\right) - \varphi_{\text{set}} - 90^\circ \tag{7}$$

From (7), the fault-point current angle can also be calculated based on the electrical quantities $\Delta\dot{I}_{mN}^1$ and $\Delta\dot{U}_{mN}^1$ on the IBRs-side.

(3) Phase-to-Phase Ground Fault

A double-phase-to-ground fault is an unsymmetrical fault, and thus the positive-sequence, negative-sequence and zero-sequence components are considered. Fig. 6 shows the fault-component equivalent network under the phase B-to-phase C ground fault.

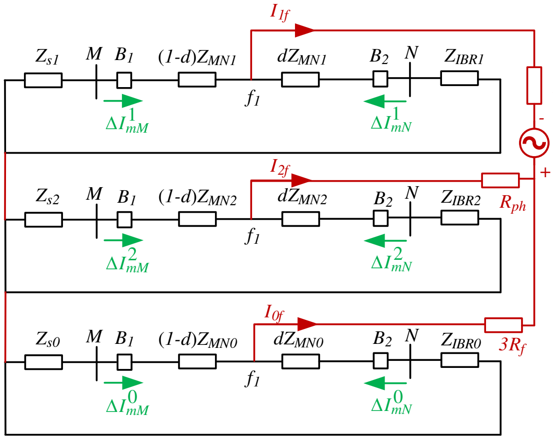

Figure 6: The fault component equivalent network under a phase-to-phase ground fault.

As shown in Fig. 6, the fault-point current under the phase-B-to-phase-C-to-ground fault can be expressed as

$$\dot{I}_f = -3\dot{I}_A^{1f} \tag{8}$$

In (8), $\dot{I}_f$ is also related to $\dot{I}_A^{1f}$. By combining (5), the expression for the phase angle of the fault-point current can be obtained as follows.

$$\arg\left(\dot{I}_f\right) = \arg\left(\Delta\dot{I}_{mN}^1 \times Z_{MN1} - \Delta\dot{U}_{mN}^1\right) - \varphi_{\text{set}} - 180^\circ \tag{9}$$

(4) Single-Phase-to-Ground Fault

A single-phase ground fault is an unsymmetrical fault, and thus the positive-sequence, negative-sequence and zero-sequence components should be considered. Fig. 7 shows the fault-component equivalent network under a phase-A ground fault. Combined with Fig. 7, $\dot{I}_f$ and $\dot{I}_A^{1f}$ satisfy $\dot{I}_f = 3\dot{I}_A^{1f}$. Following the above analysis, the expression for the fault-point current can be derived as

$$\arg\left(\dot{I}_f\right) = \arg\left(\Delta\dot{I}_{mN}^1 \times Z_{MN1} - \Delta\dot{U}_{mN}^1\right) - \varphi_{\text{set}} \tag{10}$$

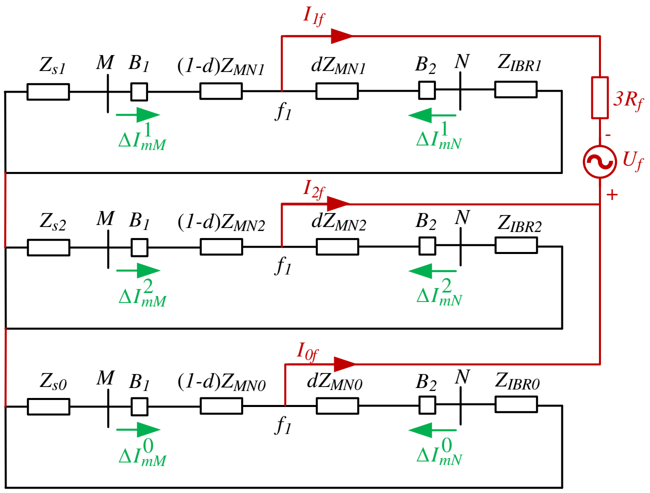

Figure 7: The fault component equivalent network under a single-phase-to-ground fault.

From the preceding derivations, the fault-point current angles under different fault types can be calculated based on $\Delta\dot{I}_{mN}^1$ and $\Delta\dot{U}_{mN}^1$. The expressions for the current reference values can be obtained, as listed in Table 1.

As shown in Table 1, the current references for IBRs inverter control can be obtained using the locally measured $\Delta\dot{I}_{mN}^1$ and $\Delta\dot{U}_{mN}^1$. Under the proposed control strategy, the angle of $\dot{I}_{mN}$ is always aligned with that of $\dot{I}_f$, thereby the additional impedance angle is always zero. If the angle is zero, the reactance component of the measured impedance becomes independent of both the fault resistance and the inverter control strategy.

Table 1: The positive-sequence current references under different fault types.

Fault Type	i_{dref}^{+} **and** i_{qref}^{+}
Three-phase fault	$i_{dref}^{+} = I_{\max}\|\cos\left[\arg\left(\Delta\dot{I}_{mN}^{1} \times Z_{MN1} - \Delta\dot{U}_{mN}^{1}\right) - \varphi_{\text{set}} - \theta_{v}^{+}\right]\|$ $i_{qref}^{+} = i_{dref}^{+}\tan\left[\arg\left(\Delta\dot{I}_{mN}^{1} \times Z_{MN1} - \Delta\dot{U}_{mN}^{1}\right) - \varphi_{\text{set}} - \theta_{v}^{+}\right]$
Single-phase fault	$i_{dref}^{+} = I_{\max}\|\cos\left[\arg\left(\Delta\dot{I}_{mN}^{1} \times Z_{MN1} - \Delta\dot{U}_{mN}^{1}\right) - \varphi_{\text{set}} - \theta_{v}^{+}\right]\|$ $i_{qref}^{+} = i_{dref}^{+}\tan\left[\arg\left(\Delta\dot{I}_{mN}^{1} \times Z_{MN1} - \Delta\dot{U}_{mN}^{1}\right) - \varphi_{\text{set}} - \theta_{v}^{+}\right]$
Phase-to-phase fault	$i_{dref}^{+} = I_{\max}\|\cos\left[\arg\left(\Delta\dot{I}_{mN}^{1} \times Z_{MN1} - \Delta\dot{U}_{mN}^{1}\right) - \varphi_{\text{set}} - 90^{\circ} - \theta_{v}^{+}\right]\|$ $i_{qref}^{+} = i_{dref}^{+}\tan\left[\arg\left(\Delta\dot{I}_{mN}^{1} \times Z_{MN1} - \Delta\dot{U}_{mN}^{1}\right) - \varphi_{\text{set}} - 90^{\circ} - \theta_{v}^{+}\right]$
Phase-to-phase-to ground fault	$i_{dref}^{+} = I_{\max}\|\cos\left[\arg\left(\Delta\dot{I}_{mN}^{1} \times Z_{MN1} - \Delta\dot{U}_{mN}^{1}\right) - \varphi_{\text{set}} - 180^{\circ} - \theta_{v}^{+}\right]\|$ $i_{qref}^{+} = i_{dref}^{+}\tan\left[\arg\left(\Delta\dot{I}_{mN}^{1} \times Z_{MN1} - \Delta\dot{U}_{mN}^{1}\right) - \varphi_{\text{set}} - 180^{\circ} - \theta_{v}^{+}\right]$

It is worth emphasizing that the derivations above strictly rely on the assumption $|Z_{s1}| << |Z_{IBR1} + Z_{MN1}|$, which accurately characterizes the fault current distribution when the IBR is connected to a strong grid. However, under weak grid conditions or scenarios with extremely high penetration of inverter-based resources, the grid-side impedance Z_{s1} may no longer be negligible. In such cases, the calculation of the fault-point current angle via (5), (7), (9), and (10) may introduce errors, potentially affecting the angle tracking accuracy of the control strategy and the reliability of the protection criterion.

To evaluate the applicability of the proposed method under these challenging conditions, the simulation studies in Section 5 will further investigate the angle tracking performance and protection behavior under weak grid and high IBR penetration scenarios, thereby demonstrating the robustness and limitations of the proposed strategy.

4 A Novel Single-Ended Protection Strategy

4.1 Protection Principle

Under the mentioned control strategy, the current angle provided by the IBRs is dynamically altered in order to align the angle of $\dot{I}_{mN}$ with $\dot{I}_{f}$. As a result, the additional impedance angle becomes zero. The measured impedance expression of relay B_2 shown in Fig. 3 is given as follows.

$$Z_{mN} = Z_{Nk} + R_{f} = \left(R_{Nk} + \left|\frac{\dot{I}_{f}}{\dot{I}_{\text{mN}}}\right| R_{f}\right) + jX_{Nk} \tag{11}$$

where R_{Nk} is the resistive component of the faulted line's actual impedance; X_{Nk} is the reactive component of the measured impedance, and is equal to the reactive component of the faulted line's actual impedance.

Fig. 8 shows the measured impedance characteristics under internal and external faults. As shown in Fig. 8, the measured impedance variation depends on the fault resistance R_f and the current amplitude ratio of $\dot{I}_{f}$ to $\dot{I}_{mN}$.

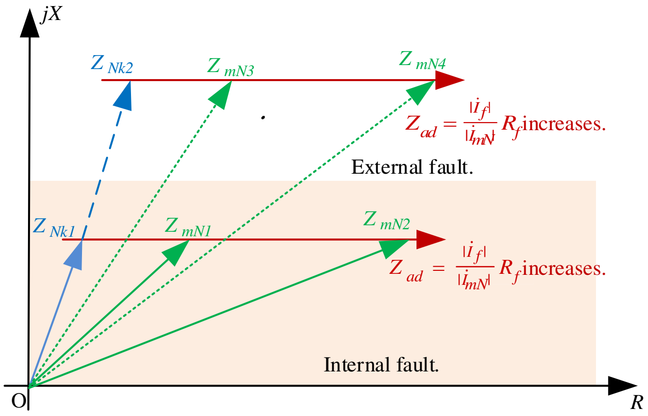

Figure 8: The measured impedance characteristics under internal and external faults.

Under internal faults, the measured impedance increases with rising R_f and the ratio. Its core characteristic is that the resistance component increases while the reactance component of the measured impedance remains constant, which corresponds to the actual reactance of the faulted line's actual impedance. Under external faults, the measured impedance shows a similar trend to that under internal faults. However, the reactance component of the measured impedance under external faults differs significantly from that under internal faults. Specifically, the reactance component maintains a smaller constant under internal faults and a larger constant under external faults. The reactance component of the measured impedance directly corresponds to the reactance component of the faulted line's actual impedance and can effectively characterize the actual fault distance. Therefore, based on the difference in the reactance component of the measured impedance between internal and external faults, a single-ended protection principle immune to the additional impedance is developed as follows.

$$0 \leq \mathrm{Im}\left(Z_{mN}\right) \leq \mathrm{Im}\left(Z_{set}\right) \tag{12}$$

where $\mathrm{Im}\left(Z_{set}\right)$ is the reactance component of the setting impedance, typically chosen as 80%–90% of the protected line's full impedance. The protection operating principle is defined as follows:

Forward internal fault ($0 \leq \mathrm{Im}\left(Z_{mN}\right) \leq \mathrm{Im}\left(Z_{set}\right)$): A fault is determined to be within the protection zone. The device issues an instantaneous trip command.

Reverse fault ($\mathrm{Im}\left(Z_{mN}\right) < 0$): The device is blocked reliably to prevent maloperation.

Forward external fault ($\mathrm{Im}\left(Z_{mN}\right) > \mathrm{Im}\left(Z_{set}\right)$): The fault is considered to be beyond the Zone I reach. No instantaneous trip is issued; it is left for time-delayed backup zones.

Although the proposed reactance principle accurately locates faults and mitigates the additional impedance interference, the performance can be adversely affected by boundary conditions, IBR fluctuations and system oscillations. To overcome these shortcomings, two auxiliary criteria are proposed to improve protection performance as follows.

Auxiliary Criterion 1: To mitigate the risks of maloperation for the main protection criterion under IBRs output current fluctuations and transient disturbances, A starting criterion using abrupt current changes on the high-voltage side of the transformer and the voltage at grid-connected bus N is proposed in Section 4.2. If the criterion is satisfied, the main protection and identification strategy is activated; otherwise, the protection is blocked.

Auxiliary Criterion 2: To solve the maloperation and poor selectivity of the pure reactance criterion at the protection zone boundary, under high-resistance faults and control-protection coordination failure, a simple resistance threshold criterion is proposed, which can be expressed as:

$$R_m^* = X_{mN} \cdot K_R + \Delta R_{\max} \tag{13}$$

where K_R is the ratio of the positive-sequence resistance to the positive-sequence reactance per unit length of the protected line; $\Delta R_{\max} = 10 - 30\ \Omega$ is set considering additional resistances from fault transition, IBRs integration and so on. When the measured reactance lies outside the operating region at the end of the protection range, the measured resistance acts to reliably block the main criterion and prevent maloperation, so as to improve the security and selectivity of the protection.

4.2 Flowchart of the Proposed Protection Strategy

The proposed control-protection coordination strategy is implemented through the process illustrated in the Fig. 9. This strategy comprises four main stages: start-up criterion fault phase selection, control strategy switching, fault current calculation, and protection criterion. The detailed analysis is provided as follows.

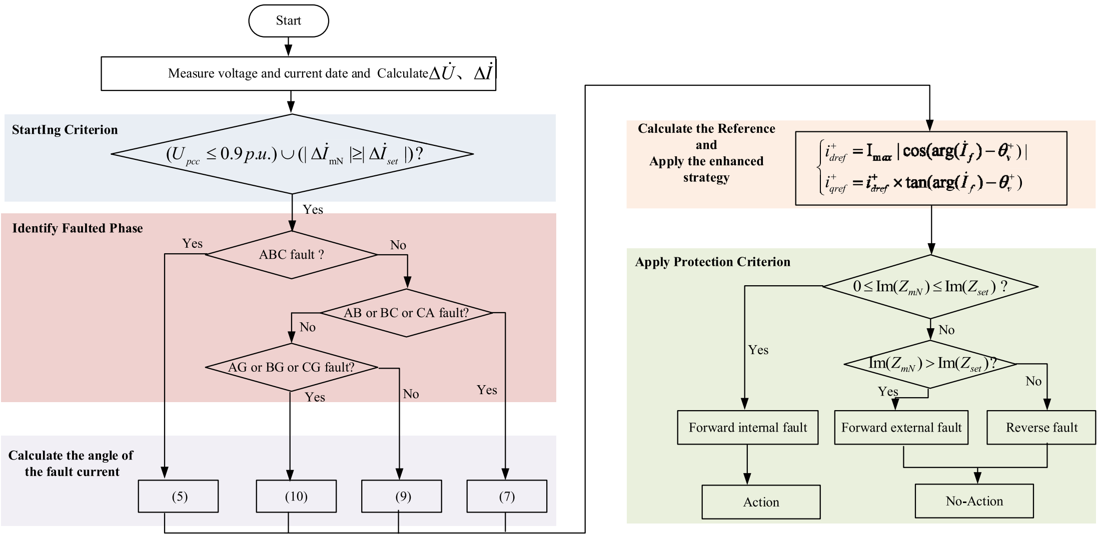

Figure 9: The control-protection coordination flowchart proposed in this paper.

(1) Evaluate Starting Criteria

To ensure reliable activation of the proposed control-protection coordination scheme while maintaining sensitivity for both metallic and high-resistance faults, a composite starting criterion based on local electrical quantities is developed. The criterion employs an "OR" logic between the undervoltage and overcurrent conditions, as expressed in (14):

$$\left(U_{pcc} \le 0.9\,\text{p.u.}\right) \cup \left(|\Delta\dot{I}_{\text{mN}}| \ge |\Delta\dot{I}_{set}|\right) \tag{14}$$

where the voltage threshold is set at 0.9 p.u. in accordance with typical low-voltage ride-through standards. The current variation threshold $|\Delta\dot{I}_{set}|$ is set above the maximum load fluctuation during normal operation to avoid nuisance trips caused by load switching or other non-fault transients.

The proposed protection starting criterion employs the OR logic of undervoltage and overcurrent criteria, which are complementary under various fault conditions. For high-resistance faults with weak voltage drops, the overcurrent criterion can effectively improve the starting sensitivity. In contrast, under weak grid conditions and high IBR penetration scenarios where the fault current is relatively low, the undervoltage criterion guarantees reliable starting. Furthermore, the criterion is identified using electrical data within only 1–2 fundamental frequency cycles, which can not only achieve fast response but also avoid misjudgment caused by normal system disturbances. The combined logic thus ensures high sensitivity and reliability under diverse operating conditions.

Once the starting criterion is satisfied, the adaptive phase control strategy described in Section 3 is immediately activated, and the distance protection element is triggered to enter the fault identification process. Simulation results in Section 5 will verify the effectiveness and reliability of the proposed starting criterion under disturbance scenarios.

(2) Identify Faulted Phase

Rapid and accurate identification of the fault type is the foundation for all subsequent analysis and control. Traditional phase selection elements are predominantly based on the principle of phase current difference variation, whose effectiveness relies on a significant difference in current variation between the faulted phases and the healthy phases. However, constrained by the internal control strategies of inverters, the short-circuit current exhibits characteristics such as limited magnitude and controlled phase. This results in a small magnitude and gradual change in the short-circuit current contributed from the PV side, which severely reduces the sensitivity or even causes the failure of traditional phase selection methods based on current variation.

To address this issue, this paper proposes a novel fault phase selection method based on the local phase-to-phase voltage difference variation combined with zero-sequence voltage at the protection installation point. The system voltage is primarily dominated by the strong system-side source and is relatively less affected by the weak-infeed PV plant. During fault transients, it can exhibit clearer and more robust asymmetry characteristics, thus providing a new criterion basis for reliable phase selection. The method is logically straightforward and is detailed as follows.

First, the presence of a ground fault is distinguished by detecting the magnitude of the zero-sequence voltage $|\Delta\dot{U}_0|$ exceeds the setting threshold ε_0 (set to avoid the maximum unbalance voltage during normal operation), a ground fault is determined; otherwise, it is a non-ground fault. If a ground fault is identified, the specific faulted phase(s) are further identified based on the relative magnitude relationships among the three phase-to-phase voltage difference variations $|\Delta\dot{U}_{AB}|$, $|\Delta\dot{U}_{BC}|$ and $|\Delta\dot{U}_{CA}|$. The criteria are:

(a) If $(m_1|\Delta\dot{U}_{BC}| \le |\Delta\dot{U}_{AB}|)$ and $(m_1|\Delta\dot{U}_{BC}| \le |\Delta\dot{U}_{CA}|)$, it is identified as an A-phase-to-ground fault (AG).
(b) If $(m_1|\Delta\dot{U}_{CA}| \le |\Delta\dot{U}_{BC}|)$ and $(m_1|\Delta\dot{U}_{CA}| \le |\Delta\dot{U}_{AB}|)$, it is identified as a B-phase-to-ground fault (BG).
(c) If $(m_1|\Delta\dot{U}_{AB}| \le |\Delta\dot{U}_{CA}|)$ and $(m_1|\Delta\dot{U}_{AB}| \le |\Delta\dot{U}_{BC}|)$, it is identified as a C-phase-to-ground fault (CG).

If none of the above conditions are met, a double-phase-to-ground fault is determined. Then, based on the maximum value among the three phase-to-phase voltage difference variations:

(d) If $(|\Delta\dot{U}_A| \ge |\Delta\dot{U}_C|)$ and $(|\Delta\dot{U}_B| \ge |\Delta\dot{U}_C|)$ is the maximum, it is identified as an AB-phase-to-ground fault (ABG).
(e) If $(|\Delta\dot{U}_B| \ge |\Delta\dot{U}_A|)$ and $(|\Delta\dot{U}_C| \ge |\Delta\dot{U}_A|)$ is the maximum, it is identified as a BC-phase-to-ground fault (BCG).
(f) If $(|\Delta\dot{U}_A| \ge |\Delta\dot{U}_B|)$ and $(|\Delta\dot{U}_C| \ge |\Delta\dot{U}_B|)$ is the maximum, it is identified as a CA-phase-to-ground fault (CAG).

For a non-ground fault, the phase-to-phase short-circuit type is identified according to the following rules:

(g) If ($m_2|\Delta\dot{U}_C| \le |\Delta\dot{U}_A|$) and ($m_2|\Delta\dot{U}_C| \le |\Delta\dot{U}_B|$), it is identified as an AB phase-to-phase fault (AB).
(h) If ($m_2|\Delta\dot{U}_A| \le |\Delta\dot{U}_B|$) and ($m_2|\Delta\dot{U}_A| \le |\Delta\dot{U}_C|$), it is identified as a BC phase-to-phase fault (BC).
(i) If ($m_2|\Delta\dot{U}_B| \le |\Delta\dot{U}_A|$) and ($m_2|\Delta\dot{U}_B| \le |\Delta\dot{U}_C|$), it is identified as a CA phase-to-phase fault (CA).

In the above criteria, the setting coefficients m_1 and m_2 are set to 1.5 and 4, respectively. This method relies solely on local voltage quantities, effectively overcoming the influence of PV-side current weak-infeed characteristics, and provides adaptive and reliable fault type information for subsequent protection and control stages.

The robustness of the proposed phase selection method based on voltage variations is systematically analyzed from three aspects: measurement noise interference, the grid disturbances, and operating conditions with different transition resistances.

In the presence of measurement noise, the criterion for single-phase-to-ground faults is applied to select fault phases through amplitude comparison between voltage variations of sound phases and voltage differences of sound-faulty phase pairs. Small and irregular random voltage fluctuations are produced by noise in each phase. The core voltage characteristics are not changed, and the relative amplitude relationship is not damaged either. The criterion for phase-to-phase faults is adopted to identify faults through amplitude comparison between the voltage variation of the sound phase and those of the two faulty phases. Fault characteristics that voltage variations of faulty phases are much larger than those of the sound phase are not fabricated by noise. Only small and irregular disturbances are introduced, and the amplitude comparison logic of the criteria is not affected. Misjudgments caused by noise are avoided for both criteria, and favorable robustness is obtained.

Under the grid disturbances, synchronous small-amplitude fluctuations of three-phase voltages are caused. The phase-to-phase voltage difference characteristics required by single-phase-to-ground fault criteria are not formed, so the operation conditions of the criterion are not satisfied. The characteristic that voltage variations of faulty phases are obviously larger than those of the sound phase required by phase-to-phase fault criteria is not presented, so the criterion is not activated. Thus, misoperation caused by grid disturbances is effectively avoided for both phase selection criteria.

Under conditions with different transition resistances, the voltage of the faulty phase drops greatly in single-phase-to-ground faults with low transition resistance, and the corresponding phase-to-phase voltage difference is quite distinct. The amplitude of voltage variations is reduced in faults with high transition resistance, but the relative phase-to-phase voltage difference is still identified effectively. The sensitivity of the criterion is reduced only in faults with extremely high transition resistance due to the loss of voltage characteristics. In phase-to-phase faults with low transition resistance, the voltage of faulty phases drops significantly, and the gap of voltage variations between faulty phases and the sound phase is clearly distinguished. The amplitude gap is narrowed in faults with high transition resistance but still meets the requirement of identification. The criterion fails only in faults with extremely high transition resistance because of indistinct voltage characteristics. Such a limitation is shared by all phase selection methods based on voltage characteristics.

Simulation studies in Section 5 will verify the effectiveness and robustness of the proposed phase selection approach under the typical grid disturbance of load switching and high transition resistance.

(3) Activate the Enhanced IBR Control Strategy

Following protection startup and fault phase selection, the enhanced IBR control strategy described in Section 3 is activated. First, the protection device captures the voltage and current data at the point of common coupling before and after the fault, extracting the positive-sequence fault components $\Delta\dot{U}_{mN}^{1}$ and $\Delta\dot{I}_{mN}^{1}$. Subsequently, based on local system parameters and the fault type identified in the previous step, the corresponding analytical model is invoked to calculate the real-time phase angle of the fault current, $\arg\left(\dot{I}_f\right)$.

The switching process follows the conventional low-voltage ride-through control framework: the outer-loop controllers (e.g., DC voltage control and reactive power control) are first blocked, and the positive-sequence current references for the inner current loop are switched to i_{dref}^{+} and i_{qref}^{+}, calculated from the expressions in Table 1. Using the calculated fault current angle together with the voltage angle θ_v^{+} obtained from the local phase-locked loop, the d-axis and q-axis reference values are computed online. The inverter then dynamically adjusts its output current angle $\arg\left(\dot{I}_{mN}\right)$ to actively track $\arg\left(\dot{I}_f\right)$, thereby forcing the additional impedance angle α_{ad} to zero.

To ensure a smooth control mode transition and maintain inverter stability during the fault transient, a gradual reference transition scheme is employed. Specifically, the calculated current references are passed through a first-order low-pass filter before being fed into the current inner loop, thereby mitigating current surges and oscillations that may arise from abrupt reference changes. The filter time constant is selected as 1–2 ms, which provides sufficient dynamic response while effectively attenuating high-frequency noise. In addition, the PI controllers in the current loop are equipped with anti-windup protection to prevent overshoot and oscillations caused by integrator saturation during reference variations. Furthermore, all current references are strictly limited to the inverter's maximum allowable current I_{max} to ensure the safe operation of power devices.

It is worth noting that the control structure remains unchanged before and after the switching process—both are based on vector control in the synchronous reference frame—and only the reference calculation method is altered. Consequently, the stability of the control loop is inherently maintained. The entire switching process is completed within 2–3 power frequency cycles, which is compatible with the fault discrimination timeframe of the protection element and does not compromise its speed. The above mechanism ensures a smooth and fast switching process, and its dynamic response characteristics, as well as control stability under various fault scenarios, will be demonstrated in the subsequent simulation analysis.

(4) Apply Protection Criterion

With $\alpha_{ad} \approx 0^\circ$ achieved, the additional impedance introduced by the transition resistance is constrained to be purely resistive, and its interference with the measured impedance is confined solely to the resistance axis. Under this condition, the measured reactance X_{mN} accurately represents the actual line reactance from the protection installation point to the fault location. The process then transitions to the final protection decision stage: the protection device continuously calculates the updated X_{mN} and compares it with the setting value X_{Nset}. If $0 \le \mathrm{Im}\left(Z_{mN}\right) \le \mathrm{Im}\left(Z_{set}\right)$ is satisfied, a zone I internal fault is determined, and an instantaneous trip command is issued; otherwise, the logic for external or reverse faults is executed, either by reliably blocking the protection or handing over to backup protection. This completes the closed-loop workflow encompassing fault detection, real-time computation, active control, and reliable protection operation.

5 Simulation

To verify the effectiveness and reliability of the proposed protection scheme, a simulation model is established in PSCAD/EMTDC based on Fig. 1, with detailed parameters listed in Table 2. The verification in this section is organized as follows: first, the effectiveness of the proposed control strategy and the correctness of the fault phase selection method are tested (Section 5.1); then, the performance of the proposed protection criterion under different fault conditions is fully evaluated (Section 5.2).

Table 2: Key parameters of the simulation system and protection settings.

Parameter	Value
Rated Voltage	110 kV
Line Length (L_{MN})	90 km
Transformer Capacity (S_{rated})	200 MVA
Positive-Sequence Impedance (Z_1)	0.012 + j0.290 Ω/km
Zero-Sequence Impedance (Z_0)	0.39 + j1.30 Ω/km
Short-Circuit Voltage Percentage ($U_k\%$)	5%
Total Positive-Sequence Impedance (Z_{MN1})	1.08 + j26.10 Ω
System-Side Equivalent Impedance (Z_s)	0.20 + j6.20 Ω
The Setting Factor of R_2	0.85

5.1 Verification of the Proposed Control Strategy

The core of the proposed strategy is to enable $\arg\left(\dot{I}_{mN}\right)$ track $\arg\left(\dot{I}_f\right)$ in real-time through IBRs' inverter control, thereby eliminating the reactance component in the additional impedance. To verify this effect, faults including AG single-phase-to-ground, BCG double-phase-to-ground, BC phase-to-phase, and ABC three-phase short-circuit faults are simulated at a location 10 km forward from bus N at t = 2 s, with a duration of 1 s. The IBRs capacity is 15 MW. Figs. 10 and 11 respectively show the angle waveforms of $\dot{I}_{mN}$ and $\dot{I}_f$ under the conventional control strategy and the proposed strategy for different fault types.

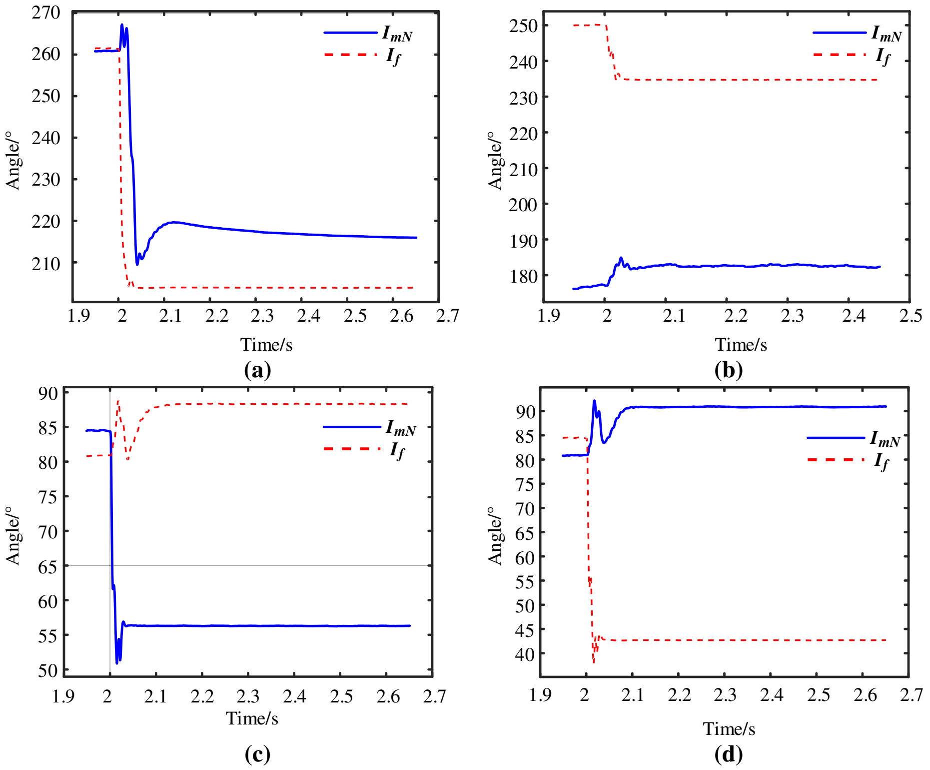

(a) (b) (c) (d)

Figure 10: Phase of short-circuit current and fault current under conventional control strategy. (**a**) ABC; (**b**) AG; (**c**) BCG; (**d**) BC.

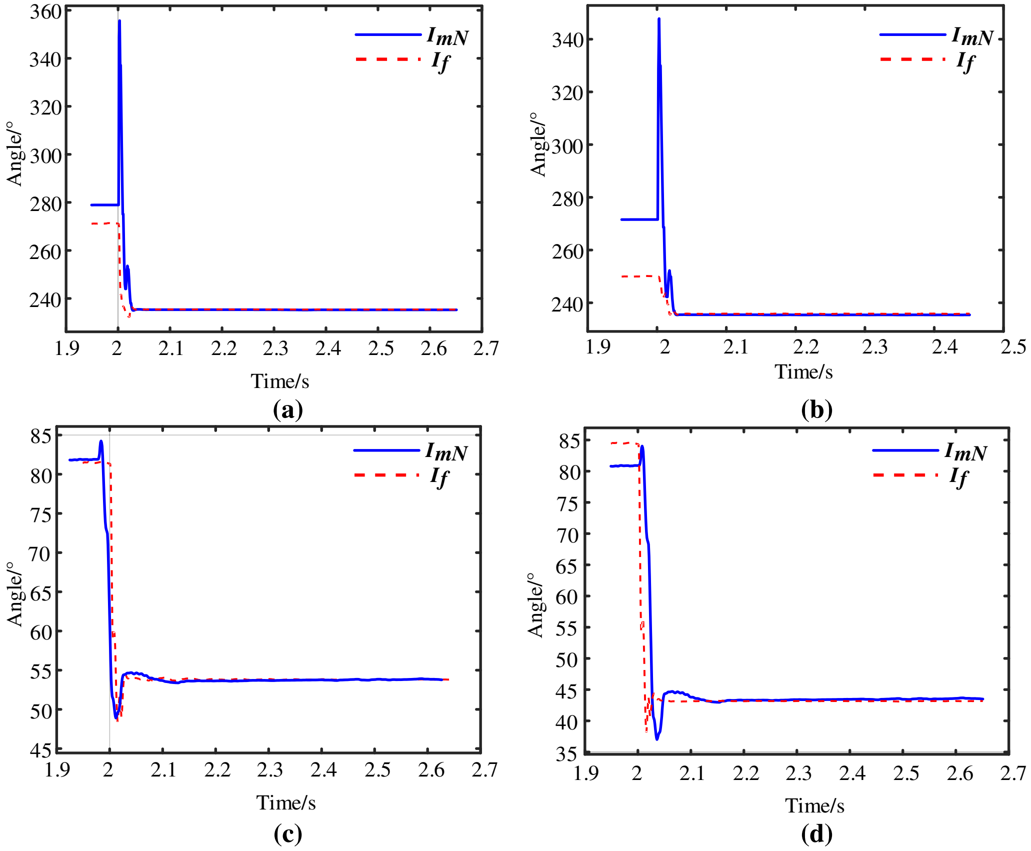

(a) (b) (c) (d)

Figure 11: Phase of short-circuit current and fault current under the control strategy proposed in this paper. (**a**) ABC; (**b**) AG; (**c**) BCG; (**d**) BC.

As illustrated in Fig. 10, a pronounced angle difference between $\dot{I}_{mN}$ and $\dot{I}_f$ is observed under the conventional control strategy under all fault conditions. The difference peaks at more than 60° for the BC fault, and reaches approximately 40° and 35° for the AG and BCG faults, respectively, which agrees well with the theoretical analysis in Section 1. Such a severe angle misalignment introduces a considerable inductive component into the additional impedance in Eq. (1), which is verified as the root cause of the measured impedance error.

In contrast, Fig. 11 illustrates that the angle waveforms of $\dot{I}_{mN}$ and $\dot{I}_f$ are nearly coincident under all fault types, the angle difference between $\dot{I}_{mN}$ and $\dot{I}_f$ approaches zero. Consequently, the proposed strategy significantly mitigates this phase difference under fault conditions.

5.2 Verification of the Single-Ended Protection Principle

5.2.1 Phase Selection Method

To verify the effectiveness of the faulted-phase selection method proposed in this paper, A fault is set 30 km ahead of bus N at t = 2 s, with 45 Ω transition resistance and 1 s duration. Table 3 lists the faulted-phase selection results.

Table 3: Phase selection results for different fault types.

Fault Type	$\lvert\Delta\dot{U}_0\rvert$	$\lvert\Delta\dot{U}_{AB}\rvert$	$\lvert\Delta\dot{U}_{BC}\rvert$	$\lvert\Delta\dot{U}_{CA}\rvert$	$\lvert\Delta\dot{U}_A\rvert$	$\lvert\Delta\dot{U}_B\rvert$	$\lvert\Delta\dot{U}_C\rvert$	Criterion Met	Phase Selection Result
AG	19.69	29.23	16.76	32.74	–	–	–	(a)	AG
BG	19.70	28.99	32.97	16.92	–	–	–	(b)	BG
CG	19.69	17.14	32.64	29.21	–	–	–	(c)	CG
ABG	16.95	48.77	31.35	31.98	24.82	40.08	10.61	(d)	ABG
BCG	16.94	48.48	32.07	31.46	10.70	24.72	39.97	(e)	BCG
CAG	16.95	31.67	32.11	38.74	40.24	10.58	24.69	(f)	CAG
AB	0	–	–	–	37.76	34.23	7.94	(g)	AB
BC	0	–	–	–	37.64	34.24	7.95	(h)	BC
CA	0	–	–	–	37.61	34.30	8.01	(i)	CA

As can be seen from Table 3, when a grounding fault occurs, the simulated zero-sequence voltage components are all significantly non-zero, which satisfies the initial criterion for identifying a grounding fault. Furthermore, by examining the phase-to-phase voltage variation data, it is observed that AG, BG, and CG faults respectively meet the relative magnitude relationships defined in criteria (a), (b), and (c) for the corresponding phase-to-phase voltage variations, thus enabling correct identification of the respective single-phase-to-ground faults. In the case of phase-to-phase-to-ground faults, ABG, BCG, and CAG faults are also accompanied by zero-sequence voltage components, and their maximum phase-to-phase voltage variations align with criteria (d), (e), and (f), respectively. Therefore, the proposed method can accurately distinguish between different types of double-phase-to-ground faults. When phase-to-phase faults occur, the zero-sequence voltage component is zero, leading the system to proceed with the non-grounding fault identification process. Here, the fault data for AB, BC, and CA satisfy criteria (g), (h), and (i), respectively, which describe the characteristic that the voltage variations between two phases are significantly larger than that of the third phase, thereby achieving reliable phase selection for the corresponding phase-to-phase short circuits. In summary, based on the criteria proposed, the simulation data for various fault types strictly trigger the corresponding judgment conditions, and the phase selection results are fully consistent with the preset fault types. This demonstrates that the proposed phase selection method based on phase-to-phase voltage variation exhibits good effectiveness and reliability under the described simulation conditions.

Table 4 shows the quantitative results under load switching disturbance and three typical faults, i.e., A-phase-to-ground (AG), phase-B-phase-C (BC), and phase-B-phase-C-to-ground (BCG). During 1.5–1.52 s after load switching, the PCC voltage remains nearly unchanged as shown in the table, while the inverter current decreases slightly owing to the constant power control of the renewable energy source; meanwhile, the starting signal and phase selection signal both keep 0 under all fault conditions, which indicates that the proposed scheme does not mal-operate under load variation and has strong immunity against load switching disturbance. When a fault occurs at 2.0 s, the PCC voltage drops obviously in Fig. 12 (consistent with the quantitative data in Table 4), the starting signal operates reliably, and the faulty phase selection result is correct, which verifies that the proposed starting and phase selection method not only avoids false operation under non-fault disturbances but also maintains reliable operating performance under various typical faults, fully demonstrating its effectiveness and robustness.

Table 4: Simulation results of voltage and operation signals under load switching disturbance.

Time Segment (s)	Quantity	AG	BC	BCG
1.4–1.5 (Pre-disturbance)	U_{pcc} (p.u.)	1.0	1.0	1.0
	Starting Signal	0	0	0
	Phase Selection Signal	0	0	0
1.5–1.52 (After load switching)	U_{pcc} (p.u.)	0.998	0.997	0.998
	Starting Signal	0	0	0
	Phase Selection Signal	0	0	0
2.0–2.3 (During fault)	U_{pcc} (p.u.)	0.611	0.372	0.712
	Starting Signal	1	1	1
	Phase Selection Signal	1	1	1

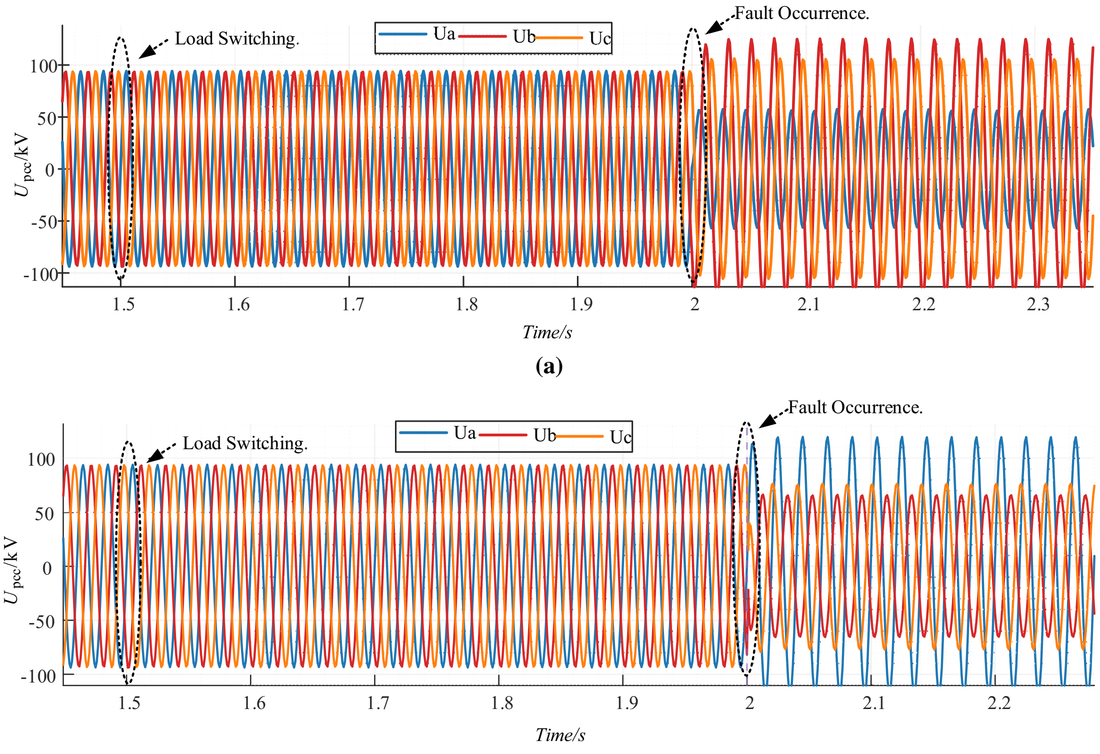

(a)

(b)

Figure 12: (Continued)

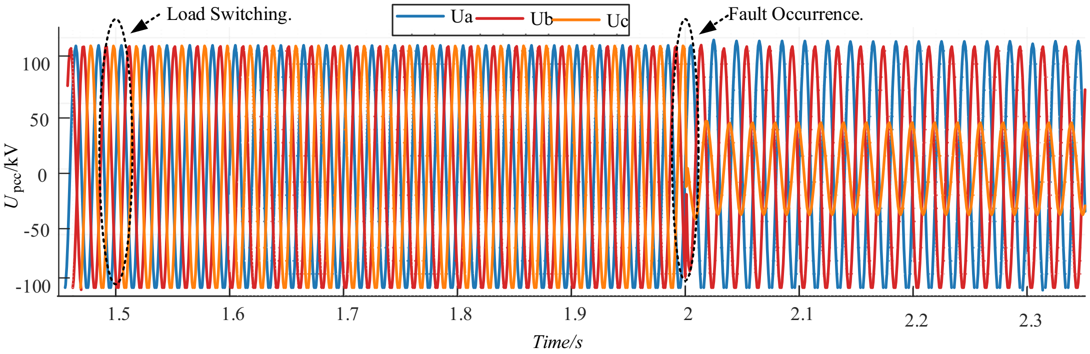

(c)

Figure 12: The PCC voltage waveforms under different fault types. (**a**) AG; (**b**) BCG; (**c**) BC.

5.2.2 Protection Performance Verification under Different Fault Scenarios

Building on the verified effectiveness of the control strategy, the operating performance of the protection criterion is further evaluated under different fault scenarios.

(1) Different Fault Locations

To assess the performance at various fault distances, different faults (ABC, BC, BCG) are applied at 10, 35, and 60 km from Bus N (t = 2 s, R_f = 35 Ω). Figs. 13–15 show the angle waveforms of $\dot{I}_{mN}$ and $\dot{I}_f$, and the reactance component of the measured impedance.

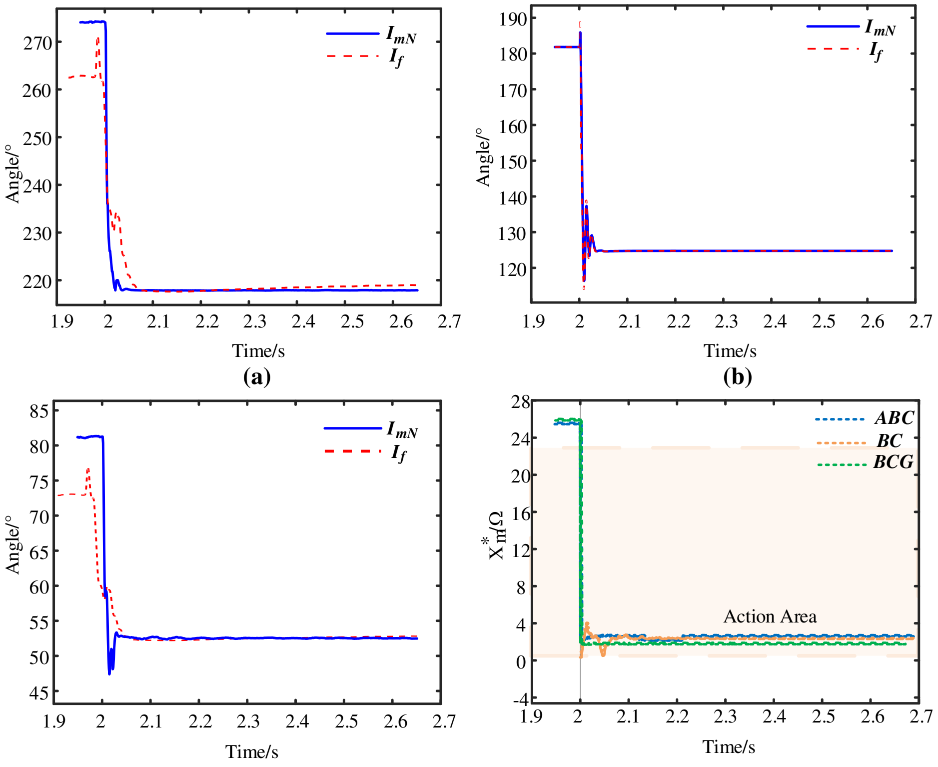

(a) (b) (c) (d)

Figure 13: Current phase and measured reactance at 10 km. (**a**) ABC; (**b**) BC; (**c**) BCG; (**d**) X_m^*.

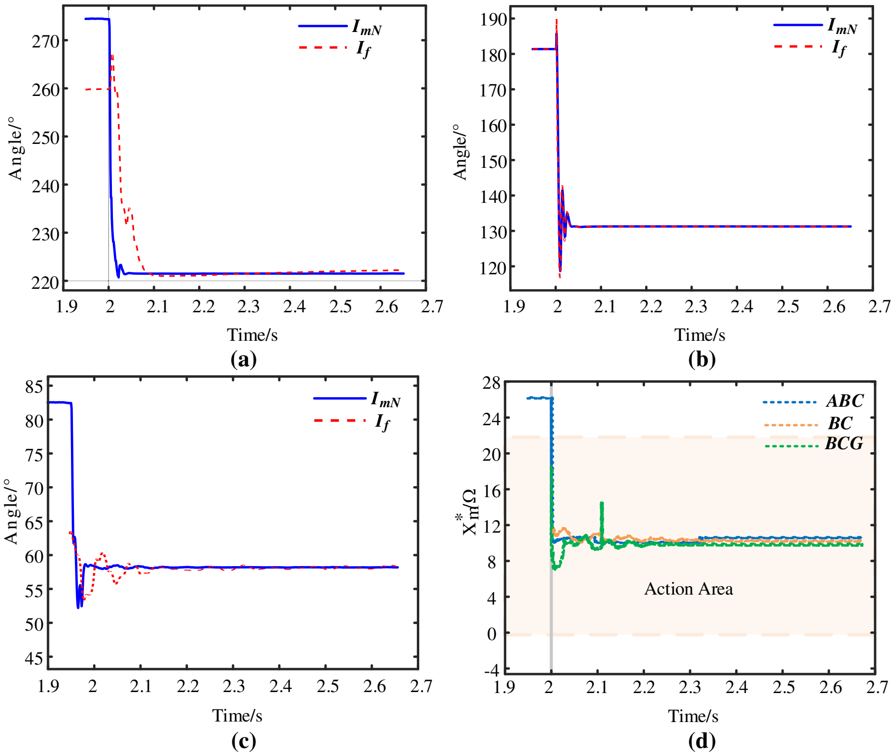

Figure 14: Current phase and measured reactance at 35 km. (**a**) ABC; (**b**) BC; (**c**) BCG; (**d**) X^*_m.

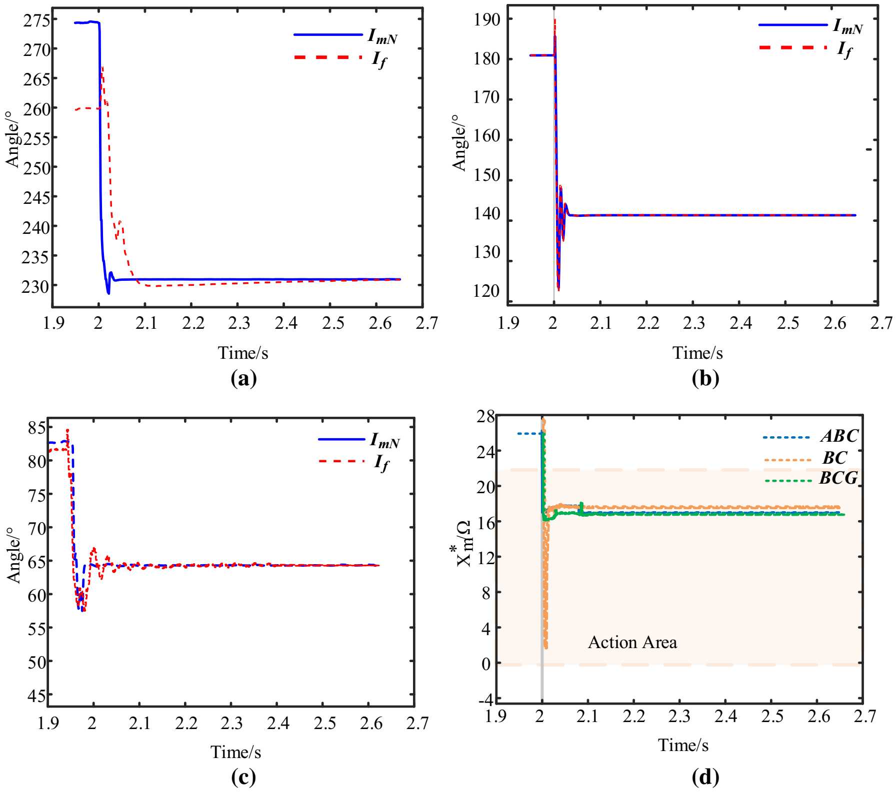

Figure 15: Current phase and measured reactance at 60 km. (**a**) ABC; (**b**) BC; (**c**) BCG; (**d**) X^*_m.

The simulation results indicate that the fault location directly affects the impedance composition of the fault loop, leading to a monotonic variation in $\arg\left(\dot{I}_f\right)$ as the distance increases. For instance, during the ABC three-phase fault, $\arg\left(\dot{I}_f\right)$ increases from 192.57° at 10 km to 229.23° at 60 km. This variation is attributed to the linear increase in line impedance with distance, which alters the overall impedance angle. However, with the proposed control strategy, accurate tracking of $\arg\left(\dot{I}_{mN}\right)$ and $\arg\left(\dot{I}_f\right)$ is achieved at all locations, as evidenced by the nearly overlapping curves in Figs. 13–15. Consequently, the simulated measured reactance X_m^* matches the theoretical values (2.9, 10.15, 17.4 Ω) calculated from line parameters. The improved distance protection operated correctly in all cases.

(2) Different Transition Resistances

Transition resistance is a key factor leading to the performance degradation of distance protection. To verify the tolerance capability of the proposed strategy, AG, BC, BCG, and ABC faults were simulated at a point 45 km from bus N in the forward direction at t = 2 s. The fault duration was 1 s, and IBR capacity was 15 MW. The transition resistance R_f was set from 0.5 Ω (metallic short-circuit) to 100 Ω (high-resistance grounding). The simulation results are shown in Table 5.

Table 5: Protection performance under different transition resistances.

R_f (Ω)	Fault Type	$\arg\left(\dot{I}_f\right)$ (°)	$\arg\left(\dot{I}_{mN}\right)$ (°)	X_m^* (Ω)	Protection Operation Status
0.5	ABC	192.57	192.72	13.05	Action
	BC	103.56	103.26	12.95	Action
	BCG	8.83	8.81	13.02	Action
	AG	223.34	223.49	13.06	Action
25	ABC	215.28	215.15	13.48	Action
	BC	130.96	131.27	13.21	Action
	BCG	49.27	40.29	13.42	Action
	AG	245.51	245.94	13.90	Action
45	ABC	229.23	229.03	13.04	Action
	BC	144.79	144.70	13.91	Action
	BCG	59.64	59.81	13.03	Action
	AG	243.77	243.64	13.96	Action
100	ABC	249.56	249.35	13.06	Action
	BC	159.19	159.11	13.85	Action
	BCG	69.11	69.51	14.09	Action
	AG	192.57	192.72	13.05	Action

As summarized in Table 5, the fault current phase exhibits a regular shift with varying transition resistance R_f, due to changes in the fault loop impedance. For a three-phase fault, $\arg\left(\dot{I}_f\right)$ increases from 192.57° to 249.56° with the increase of R_f from 0.5 to 100 Ω. The proposed strategy ensures that $\arg\left(\dot{I}_{mN}\right)$ effectively tracks this variation. The phase difference is suppressed within 0.3° across the entire R_f range (0.5–100 Ω), showing no increasing trend. Moreover, under typical high-resistance conditions (e.g., 45 Ω), precise phase synchronization is achieved for different fault types, with errors around 0.2°, based on the derived fault models. Consequently, the measured reactance X_m^* for all fault types fluctuates slightly near the actual line reactance (13.05 Ω) and remains well below the Zone 1 setting X_{Nset}, guaranteeing reliable distance protection operation.

(3) Different PV Capacities

To verify the adaptability of the proposed strategy to different IBRs capacities, faults were simulated at a point 30 km from bus N in the forward direction at t = 2 s (R_g = 30 Ω). The results are shown in Table 6.

Table 6: Protection performance under different IBRs capacities.

Capacity (MW)	Fault Type	$\arg\left(\dot{I}_f\right)$ (°)	$\arg\left(\dot{I}_{mN}\right)$ (°)	X_m^* (Ω)	Protection Operation Status
5	BC	131.25	131.79	8.94	Action
	BCG	48.59	48.45	8.12	Action
	ABC	207.30	207.77	8.54	Action
20	BC	132.15	132.23	8.98	Action
	BCG	48.94	49.55	8.86	Action
	ABC	209.14	209.26	8.92	Action
50	BC	134.05	134.33	8.67	Action
	BCG	49.67	49.70	8.74	Action
	ABC	213.46	213.22	8.79	Action
75	BC	136.24	136.37	8.61	Action
	BCG	50.40	50.41	8.64	Action
	ABC	216.35	216.68	8.48	Action

As presented in Table 6, IBRs capacity was varied from 5 to 75 MW, corresponding to an SCR range from approximately 1:20 to 1:1.33, thereby covering low- to high-penetration scenarios.

The simulation results indicate that the phase difference between $\arg\left(\dot{I}_{mN}\right)$ and $\arg\left(\dot{I}_f\right)$ does not increase with IBRs capacity. For instance, during a BC fault, $\arg\left(\dot{I}_f\right)$ changes from 131.25° to 136.24°, while $\arg\left(\dot{I}_{mN}\right)$ maintains close tracking, with a maximum phase error below 0.54°. This demonstrates that the performance of the proposed strategy is robust against varying PV output levels. Furthermore, the measured reactance X_m^* for different fault types is calculated to be between 8.1 and 9.0 Ω across the tested capacity range, all values being well below the setting X_{Nset} and closely distributed around the theoretical value of 8.7 Ω, confirming the good adaptability of the improved distance protection.

(4) Impact of Distribution Capacitance

To validate the impact of distributed capacitance on the proposed scheme in this paper, a comparative simulation is conducted. It is assumed that an AB two-phase grounding fault (ABG), an A-phase grounding fault (AG), and a three-phase short-circuit fault (ABC) occur at a distance of 35 km from bus N at t = 2.0 s, with R_g = 35 Ω for all cases. Two typical scenarios are constructed by varying the line capacitance per unit length: a high distributed capacitance scenario (positive-sequence capacitive reactance: 0.0130μ F/km, zero-sequence capacitive reactance: 0.0103μ F/km) and a low distributed capacitance scenario (positive-sequence capacitive reactance: 0.0083μ F/km, zero-sequence capacitive reactance: 0.0059μ F/km). The results are shown in Table 7.

Table 7: Protection performance under different distribution capacitance.

Scenarios	Fault Type	$\arg\left(\dot{I}_f\right)$ (°)	$\arg\left(\dot{I}_{mN}\right)$ (°)	X_m^* (Ω)	Protection Operation Status
High capacitance	ABG	61.09	60.54	10.12	Action
	ABC	274.57	274.25	10.35	Action
	AG	274.39	274.16	10.42	Action
	AB	135.51	135.01	10.45	Action
Low capacitance	ABG	60.831	60.672	10.11	Action
	ABC	214.08	214.77	9.92	Action
	AG	231.87	231.24	10.28	Action
	AB	137.91	137.54	10.37	Action

As shown in Table 7, under different distributed line capacitance conditions, $\arg\left(\dot{I}_f\right)$ closely matches $\arg\left(\dot{I}_{mN}\right)$ on the system side for various fault types. Specifically, the maximum phase difference is only 0.55° in the high-capacitance scenario and 0.93° in the low-capacitance scenario, both remaining within 1°. This further verifies the strong adaptability of the proposed method under different line parameters. Moreover, the calculated X_m^* values consistently approach the experimental reference value (10.115°) with minor fluctuations under varying capacitance conditions, and the protection operates reliably in all cases.

(5) Weak-Grid Scenarios

To further evaluate the robustness of the proposed control-protection coordination strategy under weak-grid conditions, supplementary simulations are performed with elevated grid-side equivalent impedance Z_s. Key simulation parameters are configured as: IBR capacity is 15 MW, fault resistance is 35 Ω, and fault location at 45 km ahead of bus N. All other parameters are identical to those in the strong-grid simulations described in Section 5.2.2. Two weak-grid levels are defined with Z_s = 160 Ω and Z_s = 200 Ω, respectively, both yielding a substantial reduction in short-circuit capacity relative to the strong-grid case. Under these conditions, the assumption $|Z_{s1}| << |Z_{IBR1} + Z_{MN1}|$ is no longer strictly valid, and the grid-side fault current ceases to be dominant.

As shown in Table 8, under both weak-grid configurations, the start-up criterion based on the "OR" logic is reliably triggered. Taking the voltage criterion as an example, U_{pcc} in all fault scenarios are below the threshold of 0.9 p.u. Therefore, the start-up criterion is satisfied solely by the voltage condition, without relying on the current variation. Meanwhile, the fault phase selection method correctly identifies all fault types, with the selection results for AG, BC, and BCG faults matching the actual fault types.

Furthermore, the IBR-side current angle $\arg\left(\dot{I}_{mN}\right)$ closely tracks the fault-point current angle $\arg\left(\dot{I}_f\right)$, with a maximum phase difference of approximately 1.45°. Consequently, the measured reactance X_m^* remains in the range of 13.04 to 13.11 Ω, closely matching the theoretical line reactance from the relay location to the fault point (approximately 13.05 Ω). In all test cases, the protection operates correctly, demonstrating that the proposed control-protection coordination strategy maintains satisfactory performance even when the grid impedance is significantly increased. For the typical weak grid conditions examined in this paper, the proposed method remains effective.

Table 8: Protection performance under weak-grid scenarios.

Scenarios	Fault Type	U_{pcc}	Phase Selection Result	$\arg\left(\dot{I}_f\right)$ (°)	$\arg\left(\dot{I}_{mN}\right)$ (°)	X_m^* (Ω)	Protection Operation Status
$Z_s = 160\ \Omega$	AG	0.24	AG	191.13	189.68	13.04	Action
	BC	0.42	BC	107.75	106.54	13.05	Action
	BCG	0.24	BCG	23.95	22.88	13.05	Action
$Z_s = 200\ \Omega$	AG	0.11	AG	190.29	189.29	13.11	Action
	BC	0.52	BC	112.03	110.72	13.05	Action
	BCG	0.21	BCG	24.59	23.68	13.04	Action

5.3 *Comparison with Existing Methods*

To verify the performance of the proposed distance protection scheme, it is compared with the control-protection coordination method in Ref. [27] and the adaptive distance protection method in Ref. [28]. The PV capacity is set to 15 MW unless otherwise stated. Three fault types are employed: AG, BC, and BCG. The simulation scenarios are configured as follows:

Weak-grid condition: The grid-side equivalent impedance is 160 Ω, representing low short-circuit capacity. A fault is placed 45 km from bus N with fault resistance.

High fault-resistance condition: A fault resistance is set at 45 km from bus N to test performance under high-resistance faults.

The protection operation results and analysis are listed in Table 9.

Table 9: Protection performance under different ways.

	Fault Type	Weak-Grid		High Fault Resistance	
		Protection Operation Status	Trip Instant (s)	Protection Operation Status	Trip Instant (s)
This paper	AG	Action	2.03	Action	2.03
	BC	Action	2.02	Action	2.04
	BCG	Action	2.02	Action	2.03
Ref. [27]	AG	Action	2.07	No-action	–
	BC	No-action	–	Action	2.11
	BCG	Action	2.05	Action	2.09
Ref. [28]	AG	Action	2.07	Action	2.05
	BC	Action	2.03	Action	2.05
	BCG	No-action	–	No-action	–

From Table 9, under the weak grid scenario, the operational performance of the three methods shows significant differences: the proposed method achieves 100% reliable operation for three typical faults (AG, BC, and BCG), with tripping times concentrated in 2.02–2.03 s; Ref. [27] operates reliably only for AG and BCG faults but fails to operate for BC phase-to-phase faults, with tripping times of 2.05–2.07 s. The core reason for its failure in BC faults is its reliance on dynamic phase synchronization between the IBR-side and grid-side currents. In weak grids, the fault current amplitude attenuates, and BC phase-to-phase faults lack zero-sequence components to enhance signal characteristics, leading to the loss of phase synchronization accuracy and the additional impedance being unable to maintain a pure resistive characteristic; Ref. [28] operates normally only for AG and BC faults but fails to operate for BCG double-phase-to-ground faults, with tripping times of 2.03–2.07 s. The core reason for its failure in BCG faults is its dependence on negative-sequence components to calculate the additional impedance angle. In weak grids, the grid-side negative-sequence components attenuate significantly, and BCG faults involve the superimposed interference of positive-sequence, negative-sequence and zero-sequence components, resulting in decreased separation accuracy of sequence components and calculation errors exceeding the fault tolerance threshold of the protection criterion. From the perspective of operating speed characteristics, the proposed method has the fastest operating speed and the smallest fluctuation range (only 0.01 s), which is 0.02–0.05 s faster than Ref. [27] and 0.01–0.04 s faster than Ref. [28], fully demonstrating its superior operating sensitivity and rapidity.

Under the high fault resistance scenario, the operational performance of the three methods also shows significant differences: the proposed method achieves 100% reliable operation for three typical faults (AG, BC, and BCG), with tripping times concentrated in 2.03–2.04 s; Ref. [27] operates reliably only for BC and BCG faults but fails to operate for AG faults, with tripping times of 2.09–2.11 s. The core reason for its failure in AG faults is its reliance on dynamic phase synchronization between the IBR-side and grid-side currents. In high fault resistance conditions, the transition resistance greatly suppresses the fault current and results in a sharp attenuation of the fault current amplitude. Meanwhile, the zero-sequence components for AG faults are further weakened, leading to insufficient signal characteristics for phase synchronization and a serious decline in synchronization accuracy. Therefore, the additional impedance cannot maintain a pure resistive characteristic, which results in protection failure; Ref. [28] operates normally only for AG and BC faults but fails to operate for BCG faults, with tripping times of 2.03–2.07 s. The core reason for its failure in BCG faults is its dependence on negative-sequence components to calculate the additional impedance angle. In high fault resistance conditions, the grid-side negative-sequence components attenuate further, and BCG faults involve the superimposed interference of positive-sequence, negative-sequence and zero-sequence components, leading to a significant decrease in the separation accuracy of sequence components and calculation errors exceeding the fault tolerance threshold of the protection criterion. From the perspective of operating speed characteristics, the proposed method has the fastest operating speed and the smallest fluctuation range (only 0.01 s), which is 0.05–0.08 s faster than Ref. [27] and 0.01–0.04 s faster than Ref. [28], fully demonstrating its superior operating sensitivity and rapidity. Meanwhile, reliable operation under all fault types indirectly reflects its superiority in error margin control.

In summary, the proposed method eliminates the inherent reliance of traditional schemes on phase synchronization and negative-sequence component extraction in principle. It realizes the innovative reconstruction of the protection mechanism, effectively overcomes the failure-to-operate bottleneck of the compared methods under specific fault conditions, and greatly extends the applicable range of relay protection strategies. Its tripping time is stably controlled within 2.02–2.04 s, with fast response and extremely low timing fluctuation, demonstrating superior operating rapidity and stability. In terms of fault identification, the proposed method operates reliably under all fault types, provides higher discrimination accuracy and protection sensitivity, and ensures excellent operating selectivity. Meanwhile, it maintains stable performance under extreme conditions such as weak grid and high-impedance faults, is rarely affected by changes in grid operating states and fault characteristics, and fully presents outstanding multi-scenario adaptability and robustness.

6 Conclusion

To address the inadaptability of conventional distance protection to IBR-connected lines, a novel control-protection coordination strategy is proposed. Improving the current references of IBRs' inverter control, a single-ended protection principle immune to the additional impedance is developed based on the measured fault distance. The main findings obtained through simulation tests are as follows.

(1) Under the derived current references of IBRs' inverter control, the current angle on the IBR side of the protected line equals that at the fault point, and the angle error between them is within 1°. This condition effectively ensures that the additional impedance angle remains constant, independent of IBR control strategies and fault resistance. The current references are determined solely by the electrical quantities $\Delta\dot{I}^1_{mN}$ and $\Delta\dot{U}^1_{mN}$ on the IBR side, and regardless of the fault-point current.

(2) The proposed protection principle can effectively identify various types of faults occurring at different locations along the protected line. Under the condition that the transition resistance is up to 100 Ω and the IBR capacity ratio is 1:1.33, the protection can still operate correctly and reliably. The proposed protection criterion utilizes only the voltage and current at the relay location, does not require any electrical quantities from the remote end of the protected line, and is both communication-independent and easy to implement.

(3) Although it is verified through simulations that the proposed control-protection coordinated strategy can effectively mitigate the influence of additional impedance on the measured fault distance, hardware-in-the-loop (HIL) testing is still required for future research. Meanwhile, when additional loads or other power sources are connected to the IBR side of the protected line, the effectiveness of the proposed strategy requires further verification.

Acknowledgement: Not applicable.

Funding Statement: The study is supported by the National Natural Science Foundation of China (Grant No. 52107069).

Author Contributions: The authors confirm contribution to the paper as follows: Sumei Liu: conceptualization, supervision, review & editing; Jizeng Wu: methodology, formal analysis, validation, writing—original draft; Yinghong Zhang: investigation, resources; Ran Zheng: review & editing. All authors reviewed and approved the final version of the manuscript.

Availability of Data and Materials: The data confirm that data in this study are available on request.

Ethics Approval: Not applicable.

Conflicts of Interest: The authors declare no conflicts of interest.

References

1. Gu Y, Green TC. Power system stability with a high penetration of inverter-based resources. Proc IEEE. 2023;111(7):832–53. doi:10.1109/jproc.2022.3179826.
2. Liang Y, Li W, Lu Z. Effect of inverter-interfaced renewable energy power plants on negative-sequence directional relays and a solution. IEEE Trans Power Deliv. 2021;36(2):554–65. doi:10.1109/TPWRD.2020.2984653.
3. Huynh H, Khatiwada A, Poudel B, Amiri E, Quinteros MI, Field TE, et al. Experimental analysis of transmission line protection functions in grid-connected IBR. IEEE Trans Ind Appl. 2025;61(2):2300–12. doi:10.1109/TIA.2024.3522222.
4. Jia K, Li B, Bi T. Impact of wind power integration on directional elements of transmission line distance protection. Autom Electr Power Syst. 2014;38(23):100–6. (In Chinese). doi:10.1109/apap.2011.6180418.

5. Zheng T, Liu H, Bi T. Mechanism analysis and countermeasures for maloperation of distance protection for outgoing lines from renewable power stations. Proc CSEE. 2020;40(11):3493–504. (In Chinese).
6. George N, Naidu OD, Pradhan AK. Distance protection for lines connecting converter interfaced renewable power plants: adaptive to grid-end structural changes. IEEE Trans Power Deliv. 2023;38(3):2011–21. doi:10.1109/TPWRD.2022.3231403.
7. Jalilian A, Muttaqi KM, Sutanto D, Robinson DA. Distance protection of transmission lines in presence of inverter-based resources: a new earth fault detection scheme during asymmetrical power swings. IEEE Trans Ind Appl. 2022;58(2):1899–909. doi:10.1109/TIA.2022.3146219.
8. Koloushani SM, Taher SA. Enhancing distance protection in transmission grids with high penetration of renewable energy sources through cooperative protection. IET Gener Trans Dist. 2024;18(21):3462–75. doi:10.1049/gtd2.13295.
9. Yan H, Deng H, Zheng J. An adaptive distance protection strategy for distribution networks with inverter-based distributed generation. J Electr Eng Technol. 2026;21(1):233–50. doi:10.1007/s42835-025-02449-2.
10. Liang Y, Li W, Zha W. Adaptive mho characteristic-based distance protection for lines emanating from photovoltaic power plants under unbalanced faults. IEEE Syst J. 2021;15(3):3506–16. doi:10.1109/JSYST.2020.3015225.
11. Mishra P, Pradhan AK, Bajpai P. Adaptive distance relaying for distribution lines connecting inverter-interfaced solar PV plant. IEEE Trans Ind Electron. 2021;68(3):2300–9. doi:10.1109/TIE.2020.2975462.
12. Xie Y, Zou X, Duan M, Fan F, Wang H, Liu Y. Distance protection for lines terminated by inverter-based resources compatible with various inverter control schemes. IEEE Trans Ind Electron. 2025;72(12):13151–63. doi:10.1109/TIE.2025.3577310.
13. Banaiemoqadam A, Hooshyar A, Azzouz MA. A control-based solution for distance protection of lines connected to converter-interfaced sources during asymmetrical faults. IEEE Trans Power Deliv. 2020;35(3):1455–66. doi:10.1109/TPWRD.2019.2946757.
14. Daryabar H, Abedini M, Davarpanah M. An adaptive K-factor control scheme for inverter-based resources to enhance operation of distance protection. Int J Electr Power Energy Syst. 2025;173(4):111349. doi:10.1016/j.ijepes.2025.111349.
15. Zhou Z, Yu S, Li Y, Wang X, Liu H. Analysis on incorrect operation mechanism of phase-comparison distance protection caused by power angle variation in new energy transmission via VSC-HVDC. Proc CSEE. 2023;43(5):1730–9. (In Chinese). doi:10.13334/j.0258-8013.pcsee.222160.
16. Paladhi S, Pradhan AK. Adaptive distance protection for lines connecting converter-interfaced renewable plants. IEEE J Emerg Sel Top Power Electron. 2021;9(6):7088–98. doi:10.1109/jestpe.2020.3000276.
17. Chao C, Zheng X, Weng Y, Liu Y, Gao P, Tai N. Adaptive distance protection based on the analytical model of additional impedance for inverter-interfaced renewable power plants during asymmetrical faults. IEEE Trans Power Deliv. 2022;37(5):3823–34. doi:10.1109/TPWRD.2021.3138128.
18. Xie Z, Li B, He J, Shao M, Zhou B, Wu T, et al. Error analysis and improved method of time-domain distance protection for wind power transmission lines. Int J Electr Power Energy Syst. 2024;160(4):110081. doi:10.1016/j.ijepes.2024.110081.
19. Abdelemam AM, Zeineldin H, Al-Durra A, El-Saadany EF. A positive/negative voltage sequence droop-based differential protection scheme for islanded microgrids with inverter-based DG. IEEE Trans Ind Inform. 2025;21(1):327–36. doi:10.1109/TII.2024.3452209.
20. Xue L, Mu L, Fang C, Zhu J. Research on active protection method for microgrids based on harmonic injection. IEEE Trans Smart Grid. 2025;16(1):209–22. doi:10.1109/TSG.2024.3453369.
21. Yu H, Lu Z, Liu Y, Gao Y, Wan J. Injected harmonic feature based protection scheme for active distribution networks with high proportion IIDGs. IEEE Access. 2024;12:35282–99. doi:10.1109/access.2024.3368890.
22. Zheng T, Lv W, Zhuang X, Ma J. Improved time-domain distance protection for asymmetrical faults based on adaptive control of MMC in offshore AC network. Int J Electr Power Energy Syst. 2023;152(1):109229. doi:10.1016/j.ijepes.2023.109229.

23. Zheng T, Zhang R, Lv W, Liu S. Improved time-domain distance protection based on fault active control for long transmission lines of PV/BES hybrid power generation system. Int J Electr Power Energy Syst. 2024;159(6–7):110049. doi:10.1016/j.ijepes.2024.110049.
24. Naidu OD, George N, Zubic S, Krakowski M. Time-domain-based distance protection for transmission networks: secure and reliable solution for complex networks. IEEE Access. 2023;11(1):104656–75. doi:10.1109/ACCESS.2023.3316115.
25. Chao C, Zheng X, Weng Y, Liu Z, Ye H, Liu H, et al. Collaborative solution of distance protection and dual current control for outgoing lines of inverter-based resources during line-to-line faults. IEEE Trans Smart Grid. 2024;15(4):3782–94. doi:10.1109/TSG.2024.3369767.
26. Miao Z, Zhou Y, Fan L, Wang Z. An alternative control structure for grid-following converters of inverter-based resources. IEEE Open Access J Power Energy. 2023;10:283–93. doi:10.1109/OAJPE.2023.3250668.
27. Ji L, Zhang LN, Jiang EY, Hong QT, Mi Y, Fu Y. Research on new energy active fault control to improve adaptability of distance protection. Acta Energiae Solaris Sin. 2022;43(7):22–9. (In Chinese). doi:10.19912/j.0254-0096.tynxb.2020-1245.
28. Yang G, Wang R, Wang C, Yu Y, Lu P. Principle of distance protection for new energy transmission lines based on the characteristics of negative sequence suppression strategy. Power Syst Technol. 2025. (In Chinese).